Tin sulfide supported on cellulose nanocrystals-derived carbon as a green and effective catalyst for CO2 electroreduction to formate

J Mater Sci (2023) 58:14673–14685

Chemical routes to materials

Tin sulfide supported on cellulose nanocrystals-derived carbon as a green and effective catalyst for CO_2 electroreduction to formate

Nadia Garino[1,2,*], Nicolò Monti[1], Mattia Bartoli[1,3], Candido F. Pirri[1,2], and Juqin Zeng[1,2,*]

[1] *Center for Sustainable Future Technologies @Polito, Istituto Italiano di Tecnologia, Via Livorno 60, 10144 Turin, Italy*
[2] *Department of Applied Science and Technology, Politecnico di Torino, Corso Duca degli Abruzzi 24, 10129 Turin, Italy*
[3] *Consorzio Interuniversitario Nazionale per la Scienza e Tecnologia dei Materiali (INSTM), Via G. Giusti 9, 50121 Florence, Italy*

Received: 16 March 2023
Accepted: 5 September 2023
Published online: 23 September 2023

ABSTRACT

This work reports a whole green two-step approach for the synthesis of novel catalysts for efficient CO_2 conversion. A conductive carbon support was firstly obtained via pyrolysis of cellulose nanocrystals (CNCs), and the carbon surface was successively decorated with tin sulfide (SnS) through a microwave-assisted hydrothermal process. The morphology and carbon structure were characterized by field emission scanning electron microscopy and Raman spectroscopy, and the presence of SnS decoration was confirmed by X-ray photoelectron spectroscopy and X-ray diffraction analyses. The SnS supported on CNC-derived carbon shows enhanced catalytic activity for the CO_2 conversion to formate ($HCOO^-$). Good selectivity of 86% and high partial current density of 55 mA cm^{-2} are reached at − 1.0 V vs. reversible hydrogen electrode in $KHCO_3$ electrolyte. Additionally, the mass activity of the composite catalyst achieves a value as high as 262.9 mA mg_{Sn}^{-1} for $HCOO^-$ formation, demonstrating good utilization efficiency of Sn metal. In this work, the low-cost CNC-derived carbon is evidenced to be easily decorated with metal species and thus shows high versatility and tailorability. Incorporating metal species with conductive high-surface carbon supports represents an effective strategy to realize active and stable electrocatalysts, allowing efficient utilization of metals especially the raw and precious ones.

Handling Editor: Chris Cornelius.

Address correspondence to E-mail: nadia.garino@polito.it; juqin.zeng@polito.it
E-mail Addresses: nicolo.monti@iit.it; mattia.bartoli@iit.it; fabrizio.pirri@polito.it

https://doi.org/10.1007/s10853-023-08925-2

GRAPHICAL ABSTRACT

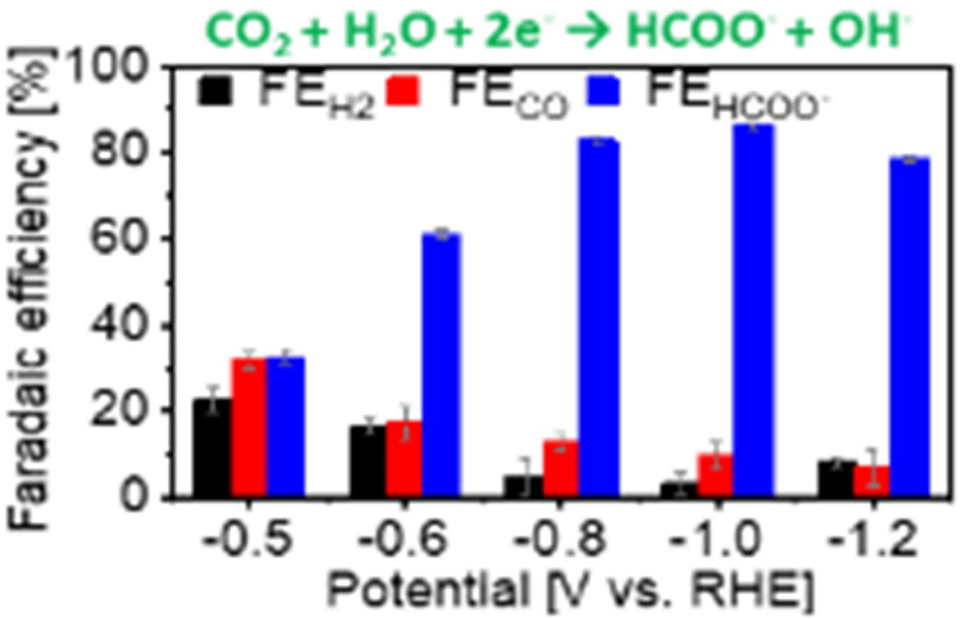

Introduction

Since the beginning of the industrial revolution, fossil fuels have become the main source for energy production [1]. As a consequence, the emission of CO_2 in the atmosphere has increased in uncontrolled way [2] causing the global warming and other climatic issues that nowadays have impact on our planet [3]. This has determined grooving efforts from the scientific community in the search of novel and effective technological solutions alternatives to fossil fuels and to mature, starting from industries, a conscious usage of raw materials [4] and, on the other hand, in developing techniques for the CO_2 capture, storage and conversion [5, 6]. In detail, the conversion of CO_2 into value-added chemicals could be considered a promising way not only to reduce the concentration of this gas in the atmosphere and to mitigate the effects of global warming but also an interesting way to monetize this process through the synthesis of valuable chemicals [7, 8]. Up to now many conversion methods have been investigated, starting from the mineralization, thermocatalysis [9, 10], photocatalytic procedures and electrochemical routes [11–13]. In particular, the electrochemical CO_2 reduction reaction (CO_2RR) demonstrates to be a quite promising route by showing many advantages such as good conversion efficiency and the overall mild conditions [14]. Due to the high reaction energy barriers, high stability of CO_2 molecule and sluggish kinetics of CO_2RR combined with the presence of many possible reaction paths that occur at similar standard potentials, the design and synthesis of specific electrocatalysts result to be fundamental steps to enhance the selectivity and the efficiency of the whole conversion process [15, 16].

Among many possible target products, formic acid/formate ($HCOOH/HCOO^-$) and carbon monoxide (CO) (or in general syngas) are the most economically feasible products [17], since they can be further converted to important raw materials for the production of various organic agent [18, 19] or used as fuel for the modern hydrogen economy [20, 21]. Various metals, alloys and metal oxides have been considered the most promising materials for the electrochemical conversion of CO_2 into $HCOOH/HCOO^-$ and syngas [22], including high-cost platinum [23], and low-cost zinc [24], copper [25, 26], bismuth [27, 28] and lead [29]. In the last years, great attention has been focused on tin-based materials [30] due to the high selectivity [31, 32] and the possibility to various synthetic routes that can tune the catalyst activity [33]. While significant progress has been made regarding the Sn-based catalysts for the CO_2RR, there are still several obstacles to overcome before nanostructured Sn-based catalysts

can be widely employed in practical applications for this purpose [34]. For example, they usually show low catalytic activity, selectivity, and durability. In addition, fundamental understanding and standard experimental systems are required to further elucidate the reaction mechanisms on Sn-based catalysts at the molecular level. Finally, green and scalable methods for synthesis are highly desired to obtain effective and low-cost electrocatalysts, paving the way for commercialization. Supporting the catalyst on high-surface area biochars represents a new strategy to stabilize nanostructures, allowing a more efficient employment of metals [24, 28, 35].

In this study we reported the easy and fast synthesis of SnS supported on a conductive and high-surface carbon support. In particular, the conductive doped carbonized cellulose nanocrystals (pCNCs) support prepared via pyrolysis [36, 37] has been considered an ideal support for the catalyst deposition because of the good electrical properties [38, 39] and high aspect ratio [40] related to the productive and purification routes used for realization [41]. Pyrolytic carbon has been found plenty of applications in material science due to their high tunability and their ability to act as template or support for catalysts and carbon species [42–44]. The subsequent modification has been carried out via a fast and reliable green microwave-assisted hydrothermal process, allowing the decoration of the carbon surface with very small SnS nanoparticles [45, 46]. The morphology and chemical composition of the SnS supported on pCNCs carbon (SnS/pCNC) were characterized by field emission scanning electron microscopy (FESEM), Raman spectroscopy, X-ray photoelectron spectroscopy (XPS) and X-ray diffraction (XRD) analyses. The electrocatalytic performance of the nanocomposite was evaluated by CO_2 electrolysis in a controlled potential mode with complete product analysis. The SnS/pCNC catalyst demonstrated promising selectivity and activity for converting CO_2 to $HCOO^-$, and it can be considered a low-cost and completely green alternative to the benchmark metal/metal oxides catalysts.

Experimental

Materials

Neat CNCs were purchased from Alberta-Pacific Forest Industries (Batch COMP170823-H). Thiourea (CAS Number: 62-56-6), tin(II) chloride dihydrate ($SnCl_2{\cdot}2H_2O$, CAS: 10025-69-1), 5 wt% solution of Nafion® 117 (CAS Number: 31175-20-9), isopropanol (CAS Number: 67-63-0), and potassium hydroxide (CAS Number: 1310-58-3) were purchased from Merck. They were used as received unless otherwise indicated.

Synthesis of carbon support (pCNCs)

Neat CNCs were pyrolyzed in a vertical furnace equipped with a quartz reactor (heating rate: 15 °C min^{-1}) and kept at 400 °C for 30 min in N_2 atmosphere. Then, the as-pyrolyzed CNCs were annealed by using a vacuum electric furnace (Pro.Ba., Cambiano, Italy) under Ar atmosphere (99.99% purity, pressure 550 mbar) using a heating rate of 2.5 °C min^{-1} and maintained at the maximum temperature of 1500 °C for 30 min in order to obtain a high crystalline carbon lattice. Then the resultant carbonaceous material (pCNC) was cooled down to room temperature by following the previously reported procedure [47].

Synthesis of carbon supported SnS (SnS/pCNC)

The decoration of pCNC was carried out through a microwave-assisted method. Typically, 350 mg of pyrolyzed CNC (pCNC) was added to 30 mL of DI water containing 140 mg of thiourea. Then, 175 mg of $SnCl_2{\cdot}2H_2O$ was added and dissolved in the as-prepared mixture by using an ultrasonic bath (Elmasonic S, Elma Schmidbauer GmbH, Singen, Germany) for 30 min. The as-obtained homogeneous dispersion was then transferred in a microwave Teflon reactor (100 mL) equipped with pressure and temperature probes (Milestone FlexyWave, Milestone Inc, Shelton, Connecticut) and irradiated for 15 min at 180 °C (maximum 800 W). The reactor was cooled down to room temperature, and the resultant suspension (SnS/pCNC) was collected, washed with DI water twice and then dried at 60 °C overnight.

Physical and electrochemical characterization

Morphological characteristics of the samples were obtained through field emission scanning electron microscopy (FESEM Supra 40, Zeiss, Oberkochen, Germany) equipped with a Si(Li)detector (Oxford

Instruments, Abington, UK) for energy-dispersive X-ray spectroscopy (EDX).

X-ray diffraction (XRD) patterns of the samples were acquired with a PANalytical X'Pert Pro diffractometer (Cu-Kα radiation, 40 kV and 30 mA) equipped with an X'Celerator detector.

The surface chemical composition was investigated by using a PHI 5000 Versaprobe Scanning X-ray Photoelectron Spectrometer (monochromatic Al K-alpha X-ray source with 1486.6 eV energy). A spot size of 100 µm was used in order to collect the photoelectron signal for both the high resolution (HR) and the survey spectra. Different pass energy values were exploited: 187.85 eV for survey spectra and 23.5 eV for HR peaks. All samples were analyzed with a combined electron and argon ion gun neutralizer system, in order to reduce the charging effect during the measurements. The semi-quantitative atomic com-positions and deconvolution procedures were obtained using Multipak 9.6 dedicated software. All core-level peak energies were referenced to C1s peak at 284.5 eV, and the background contribution in HR scans was subtracted by means of a Shirley function.

Raman spectra were collected using a Renishaw inVia (H43662 model, Gloucester-shire, UK) equipped with a green laser line (514 nm) with a 50× objective. Raman spectra were recorded in the range from 500 to 3500 cm^{-1}, and the fitting was carried out according with the previously reported procedure [48].

Residual amount of both pCNC and SnS/pCNC was investigated through thermo-gravimetric analysis (TGA) using Netzsch TG 209F1 Libra in N_2 flux (20 mL min^{-1}) with a temperature ramp of 10 °C min^{-1} from 30 to 900 °C.

Specific surface area of the samples was measured by means of N_2 sorption at − 196 °C on a micrometrics Tristar II instrument (Micromeritics Instrument Corporation, USA). Brunauer–Emmett–Teller (BET) model was used to analyze the experimental data.

Electrode preparation and electrochemical test

To prepare the electrode, 2.5 mg of synthesized catalyst, 22.5 µL of Nafion® 117 solution and 130 µL of isopropanol were well mixed and sonicated for 30 min until a uniform slurry was obtained. The slurry was then coated onto a carbon paper (GDL; SIGRACET 28BC, SGL Technologies), which is widely used as the electrode substrate to enhance the gas diffusion [49–51]. The obtained electrode was dried at 60 °C overnight to evaporate the solvents. The mass loading of the catalyst is about 1.5 mg cm^{-2}. The effect of mass loading on the electrode performance has been thoroughly studied on similar materials in our previous work [52], showing that a catalyst loading of 1.5 mg cm^{-2} can enable the fabrication of homogeneous electrodes and the simultaneous attainment of optimal mass transport.

The electrochemical reduction of CO_2 was carried out at controlled potential mode with a CHI760D electrochemical workstation. The comparison of various electrodes was carried out in 0.1 M $KHCO_3$ electrolyte in a batch cell (Fig. 1a), while the optimal catalyst was further studied in 2.0 M $KHCO_3$ in a customized flow cell (Fig. 1b). A Ag/AgCl (1 mm, leak-free LF-1) was used as the reference electrode and inserted in the catholyte. A Pt foil (Goodfellow, 99.95%) was used as the counter electrode and immersed in the anolyte. A catalyst-coated carbon paper with a geometric area of 1.5 cm^2 was used as the working electrode. A proton exchange membrane (Nafion™ Membrane N117, Sigma-Aldrich) was used to separate the anodic and cathodic compartments. In the batch cell, both anolyte and catholyte were stationary, and constant CO_2 flows of 10 and 15 mL min^{-1} was purged through the anolyte and catholyte, respectively. In the flow cell, both catholyte and anolyte were circuited at 2 mL min^{-1} during the test, and a constant CO_2 flow of 10 mL min^{-1} was purged through the anolyte, while a CO_2 flow of 25 ml min^{-1} was maintained at the gas compartment of the cathodic side. Each test has been replicated twice.

The reported potential was corrected by compensating the ohmic potential drop, of which 85% by the instrument (iR compensation). Gas-phase products

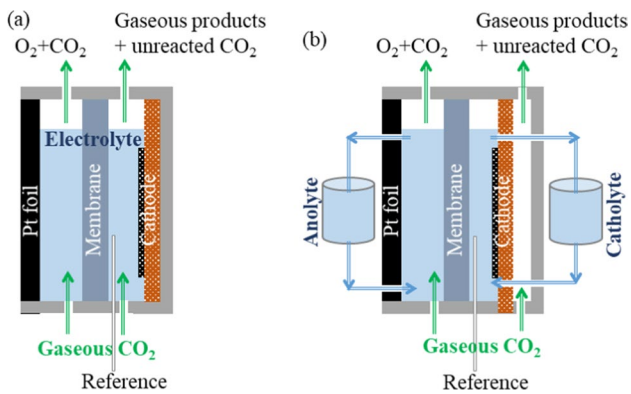

Figure 1 Illustrations of CO_2RR setups: **a** batch cell and **b** flow cell.

were analyzed online by a microgas chromatograph (μGC, Fusion®, INFICON) equipped with a micro-thermal conductivity detector, containing a 10 m Rt-Molsieve 5A column and an 8 m Rt-Q-Bond column, respectively. Liquid products were analyzed by a high-performance liquid chromatograph (Shimadzu HPLC) with a UV–Vis Detector set at 210 nm by using a ReproGel (300 × 8 mm) column, with 9.0 mM H_2SO_4 (flow rate of 1.0 mL min^{-1}) as mobile phase.

The FE for each product was calculated by dividing the charge needed to produce the actual determined amount of this product by the total charge consumed during a corresponding reduction period, as shown in Eq. 1:

$$FE = nNF/Q \quad (1)$$

where N is the amount of a detected product (number of moles, mol); n is the number of electrons required to obtain 1 molecule of this product ($n = 2$ for CO, HCOOH and H_2 formation); F is the Faraday constant (96,485 C mol^{-1}); Q is the total charge passed through the system recorded during electrolysis (coulombs, C).

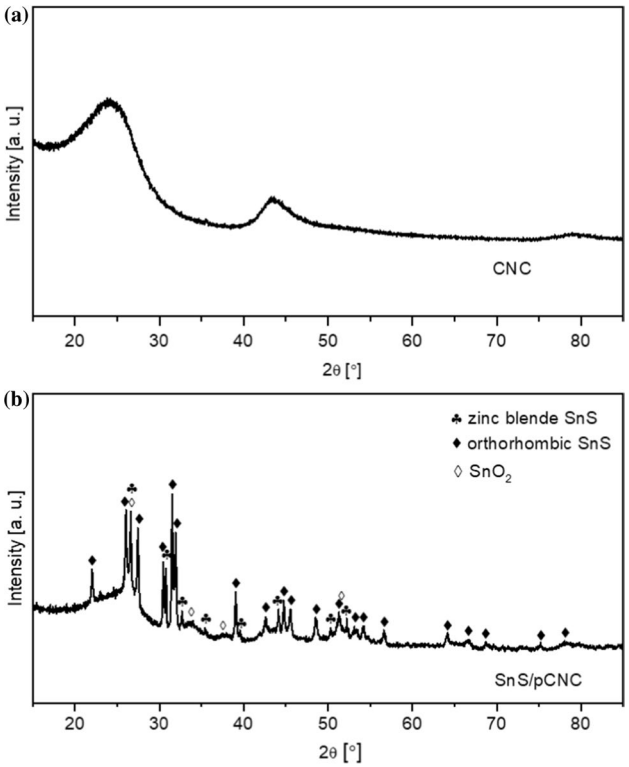

Figure 2 XRD patterns of pCNC (**a**) and SnS/pCNC (**b**).

Results and discussion

Physical and chemical characterizations

XRD analysis was firstly performed in order to understand the crystalline structure of the materials. Figure 2a, b shows the XRD patterns of pCNCs and SnS/pCNCs samples, respectively. The CNC sample shows a main diffraction peak close to 23.9° (2θ), which is related to the graphitic structure (002) plane and negatively shifted with respect the pure graphite that has a (002) peak at about 26.7° [53]. This outcome indicates that the CNC sample is composed of a large amount of disordered carbon or an amorphous phase. The SnS/pCNC sample shows well-defined peaks related to the orthorhombic crystal structure of SnS (reference code: 00-039-0354) and the structure of tetrahedral zinc blende SnS [54]. In addition, small and broad peaks related to SnO_2 with a tetragonal structure are also identified (reference code: 00-041-1445). Due to the contribution of CNC, the XRD pattern of Sn@dCNC shows a broad peak at low 2θ position (< 30°), besides the well-defined peaks for orthorhombic and zinc blende SnS and small peaks for the SnO_2. The presence of a small amount of SnO_2 could be due to the oxidation of the surface of SnS particles.

A quantitative analysis of SnS amount was further performed using TGA analysis, as shown in Fig. S1. The residue of pCNCs and SnS/pCNCs after the decomposition in air at 900 °C is 1.5 wt% and 19.4 wt%, respectively. The difference between the two residues (17.9 wt%) is reasonably due to the remaining of SnO_2 formed by SnS oxidation [55]. Accordingly, the Sn percentage is calculated to be 14.1 wt% based on the elemental composition of SnO_2 (Sn 78.7 wt%, O 21.3 wt%), and the SnS percentage in the SnS/pCNC sample is estimated to be 17.9 wt% based on the elemental composition of SnS (Sn 78.7 wt%, S 21.3 wt%).

Figure 3 shows the morphology of pCNC and SnS/pCNC samples. The pCNCs are deformed spheroids with an average diameter of 8–10 μm (Fig. 3a), and each spheroid is composed of collapsed disks of 1–2 μm with a textured surface (Fig. 3b). The surface of pCNCs displays small carbon structures of 30–100 nm, which are formed by the carbonization of organic compounds from the inner core of the CNCs during the pyrolytic conversion. As shown in Fig. 3c, SnS/pCNC does not show any appreciable modification on micrometric scale preserving the original size of the pCNCs.

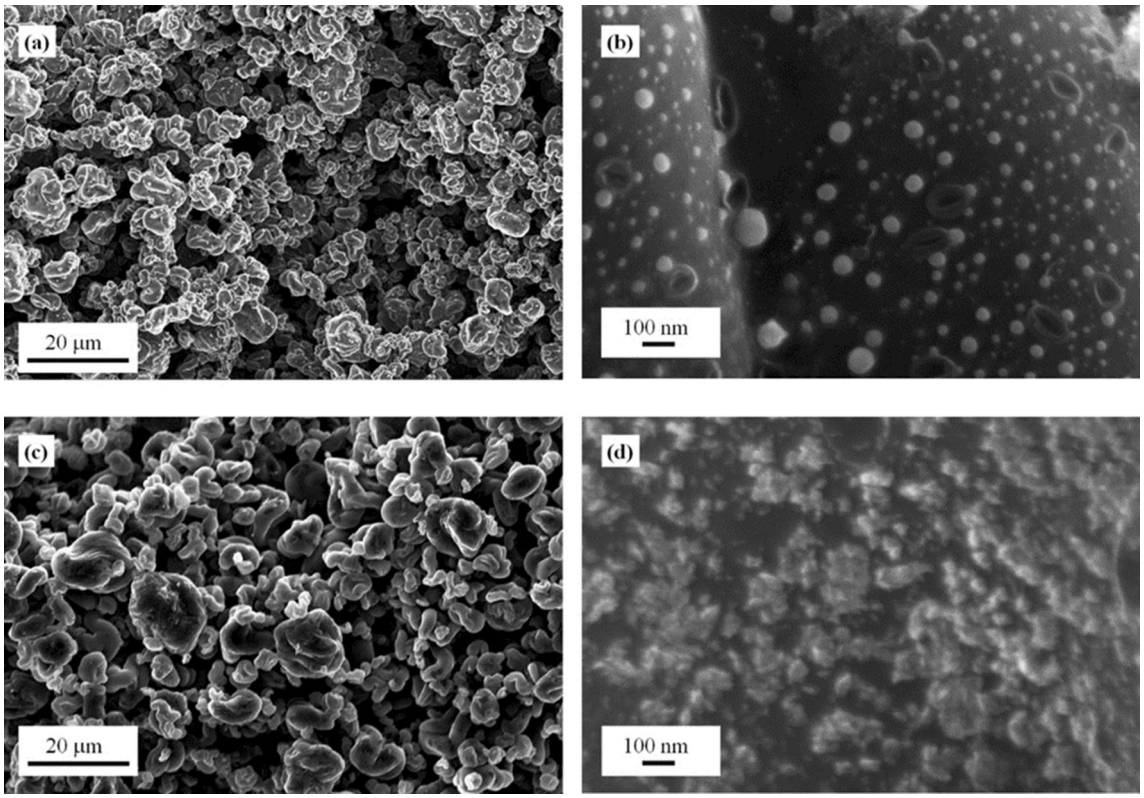

Figure 3 FESEM images at different magnifications of pCNC (**a**) and (**b**), and SnS/pCNC (**c**) and (**d**).

Nevertheless, the surface carbon texture is absent and substituted by the deposition of SnS nanoparticles as shown in Fig. 3d. The SnS particles are ranging from 20 to 30 nm, showing a polyhedral shape and a good distribution on the pCNCs surface.

As reported in Fig. S2, EDX mapping of SnS/pCNC shows a strong correlation among carbon, oxygen, and nitrogen atoms (Fig. S2b, c, e), while tin and sulfur, as well as tin and oxygen, are correlated, respectively, due to the presence of SnS and SnO_2, as indicated by XRD analysis.

Raman spectroscopy analysis was performed to evaluate the intensity ratio of the D and G bands (ID/IG ratio) [40] and the average length of graphitic clusters diameter (La) [56]. As exhibited in Fig. 4a, the pCNCs has an ID/IG ratio of 0.7 and shows a well resolved D and G peaks centered at 1349 cm^{-1} and 1578 cm^{-1}, respectively, and quite structured 2D region with three components centered at 2460 cm^{-1}, 2703 cm^{-1} and 2917 cm^{-1}, respectively. The structure of the pCNCs spectrum suggests the presence of a highly ordered graphitic like carbon [57], in good agreement with the observations in the literature [58, 59]. Accordingly, the average value of La is up to 58 Å and it is quite close to the high temperature treated biochars [35]. From SnS/pCNC spectrum in Fig. 4b, it is found that the microwave-assisted process induces the disorganization of the pCNCs increasing the ID/IG ratio up to 1.4 and reducing La down to 30 Å, reasonably due to the degradation of heteroatoms doped sp^2 clusters after the tin tailoring process [60]. This was in agreement with the increment of both pore size and surface area from the low values observed for pCNCs (surface are a 2.9 m^2/g, pore volume 0.001 cm^3/g) up to a surface are of 838.1 m^2/g, and a pore volume of up to 0.726 cm^3/g for SnS/pCNCs.

XPS analysis was performed to study the surface properties of pCNC and SnS/pCNC materials. The pCNC is mainly composed of carbon and oxygen with small amounts of nitrogen and sodium, and trace amounts of silicon and fluorine (Fig. S3a). The SnS/pCNC samples show the main presence of carbon, oxygen, sulfur and tin, with a little amount of nitrogen (Fig. 5a). The SnS/pCNCs does not show any trace of sodium, silicon and fluorine, due to their removal during the microwave process.

The high-resolution C 1*s* spectra of pCNC (Fig. S3b) show a very high amount of C sp^2 (284.6 eV)

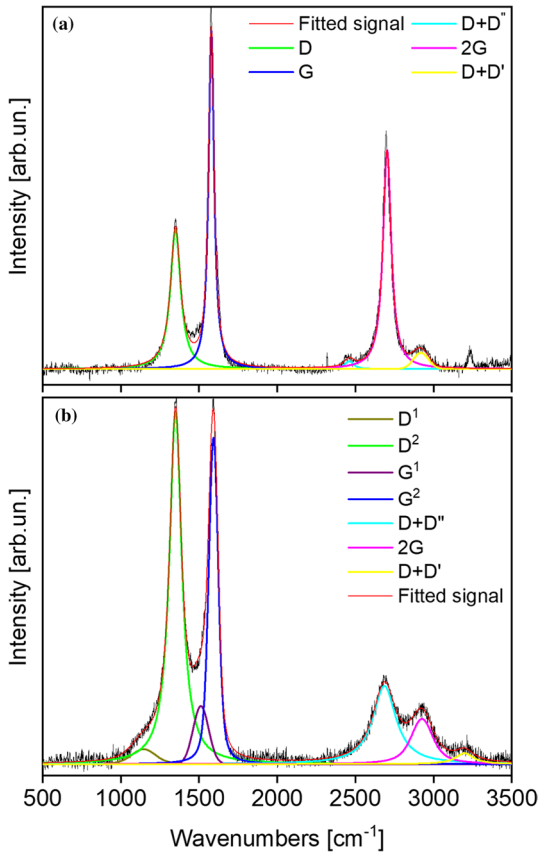

Figure 4 Raman spectra of **a** pCNCs and **b** SnS/pCNCs.

up to 85.9%, while SnS/pCNC (Fig. 5b) shows a percentage of C sp^2 up to 69.1%, as listed in Table 1. The pCNC shows also traces of C sp^3 (283.6 eV) due to edge defects and traces of C–X species (X: O, N) with a component centered at 285.9 eV. Furthermore, we detect the Auger peak at 495.9 eV of sodium (Fig. S3d), fluoride, and trace of silicon in the survey spectra of Fig. S3a. As shown in Fig. 5, SnS/pCNCs show a higher amount of C–X ratio up to 15.6% due to the activation of the carbon surface [61]. As shown in Fig. 5c, sulfur is present as thiol functions (164.7 eV) insert during the radical decomposition of thiourea [62] and also bonds to tin. As reported in Fig. 5d, the surface of SnS/pCNCs contains both SnO_2 (3*d*3/2 495.7 eV, 3*d*5/2 487.3 eV) and SnS (3*d*3/2 486.9 eV, 3*d*5/2 495.3 eV). The presence of SnO_2 could be due to the partial oxidation of SnS, in agreement with the observation by XRD.

Combining the above-mentioned analyses, a carbon support, pCNC, with a high surface area and graphitization is obtained by simply pyrolyzing the CNC biochar. The microwave-assisted hydrothermal process enables a uniform decoration of the pCNC surface with 17.9 wt% of SnS nanocrystals. The characteristics of pCNC support can assure high access to the SnS catalysts and thus guarantee good catalytic performance and high metal utilization.

Electrochemical characterization

To evaluate the catalytic activity, the SnS/pCNC sample was firstly tested in a batch cell. The pCNC was also tested for comparison. As shown in Fig. 6a, the SnS addition has a significant impact on both the selectivity and electrode activity. The pCNC electrode has low selectivity for the CO_2RR, showing about 19% of FE for CO formation and negligible FE for $HCOO^-$. Instead, the SnS/pCNC exhibits interesting selectivity for the CO_2RR, particularly toward the $HCOO^-$ formation. The good performance of the SnS/pCNC electrode is also observed at lower overpotentials, as displayed in Fig. 6b.

In order to further explore the SnS/pCNC catalyst, CO_2RR was performed in a wide range of potentials in a flow cell with 2.0 M $KHCO_3$ electrolyte. The CO_2RR in batch cells is commonly characterized by a current density lower than 10 mA cm^{-2}, due to the poor solubility of CO_2 in aqueous electrolyte [63, 64]. Instead, the flow cell configuration can enable the tests at higher current densities, since CO_2 gas is supplied directly to the electrode. At high current densities, a higher concentrated electrolyte is necessary in order to increase the ionic conductivity and reduce the ohmic overpotentials. Most importantly, a higher concentration of $KHCO_3$ leads to higher availability of CO_2 at the active sites, according to our previous study [26], which could enhance the rate and selectivity of CO_2RR. As shown in Fig. 7a, the current density increases as negatively shifting the potential. The *i*–*t* curves oscillate more significantly at higher current densities, which is attributed to the formation of more gas products and to the *i*R compensation by the potentiostat. Figure 7b shows the product distribution for the chronoamperometric tests at different potentials. $HCOO^-$ and CO are the only detected CO_2RR products with total FE values higher than 90% at low potentials (≤ − 0.8 V). The selectivity for $HCOO^-$ is comparable to the one for CO at − 0.5 V. With negatively shifting the potential, the FE_{HCOOH} is significantly enhanced, while the FE_{CO} is suppressed. The potential-dependent formate selectivity has been widely observed in the literature [65–67]. In the high potential region, HER is significant since it is thermodynamically and

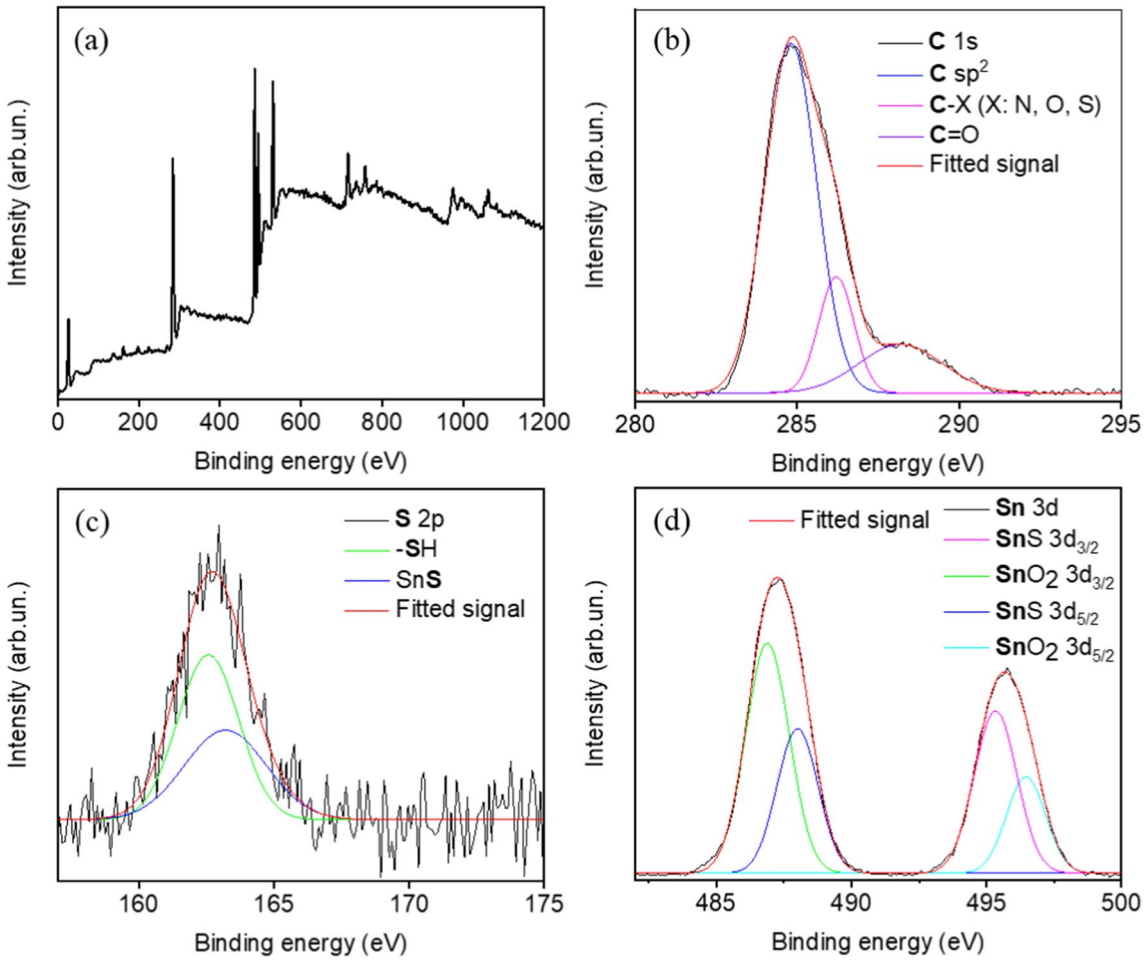

Figure 5 XPS spectra of SnS/pCNC **a** survey, **b** high-resolution spectrum of C, **c** high-resolution spectrum of S, and **d** high-resolution spectrum of Sn.

Table 1 XPS functions composition according with fitted spectra reported in Fig. 5 and Fig. S3

Sample	Carbon (%)			Oxygen (%)			Sulfur (%)		Tin (%)	
	C sp^3	C sp^2	C–X (X: O.N)	C=O	C–O	C=O	–SH	Sn–S	SnS	SnO_2
pCNCs	2.7	85.9	8.1	3.3	77.2	22.8	–	–		–
SnS/pCNCs	–	68.8	15.6	15.6	30.8	69.2	58	42	63	37

kinetically more favorable than the CO_2RR. In the low potential region, the kinetics of both CO_2RR and HER increase, while the selectivity of HER slightly increases. The slight increase at higher overpotentials could be due to the deeper reduction of tin species to metallic tin, which is reported to favor the HER [68, 69]. The highest FE_{HCOO^-} of 86% is reached at − 1.0 V, which is in line with the good results reported on $HCOO^-$-selective catalysts in the literature (Table 2). In addition, the current density for $HCOO^-$ production shows a quick increase with lowering the potential and reaches 48 mA cm^{-2} at − 1.0 V. Considering the weight percentage of Sn is about 14.1 wt% in the catalyst defined by TGA analysis, the mass activity normalized by Sn weight is presented in Fig. 7c in order to evaluate the utilization efficiency of the metal. It is noticed that the mass activity for $HCOO^-$ formation achieves as high as 262.9 mA mg_{Sn}^{-1}. Due to the high

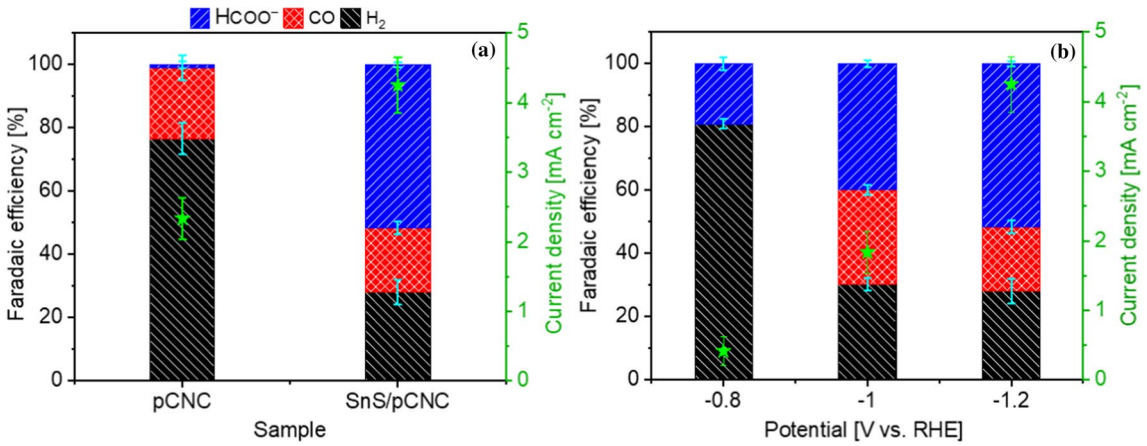

Figure 6 CO_2RR tests **a** comparison of pCNC and SnS/pCNC samples at – 1.2 V and **b** SnS/pCNC electrode at various potentials.

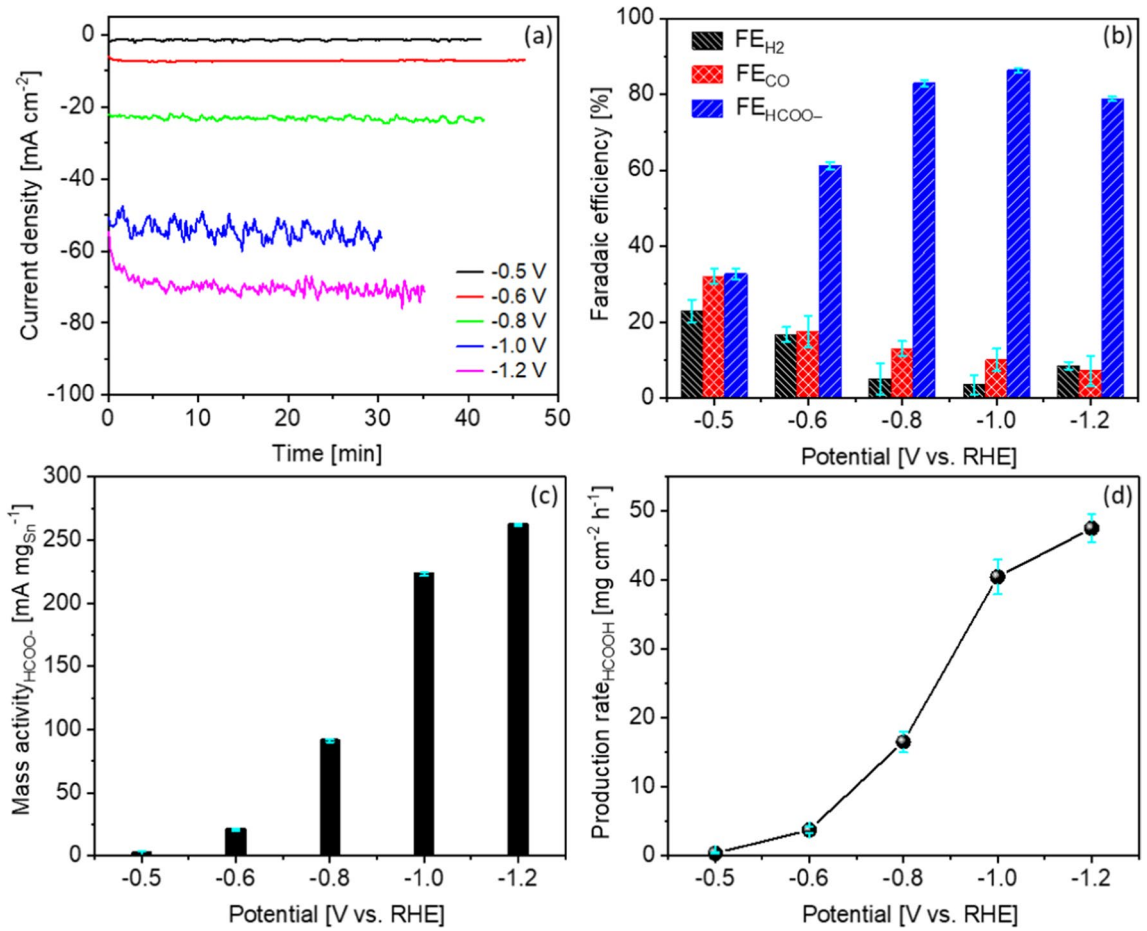

Figure 7 CO_2RR tests on SnS/pCNC electrode at various potentials **a** chronoamperometric tests, **b** selectivity of various products, **c** electrode activity normalized on the mass loading of tin metal and **d** geometric production rate of $HCOO^-$.

Table 2 Comparison of different $HCOO^-$-selective electrocatalysts in liquid-phase CO_2 electrolysis

Electrocatalyst	Electrolyte	Potential (V vs. RHE)	Current density ($-$ mA/cm^2)	FE (%)	References
SnS/pCNC	2.0 M $KHCO_3$	− 1.0	55	86	This work
nano-SnO_2/C	0.1 M $NaHCO_3$	− 1.16	6.2	86	[65]
SnO_2	0.1 M $KHCO_3$	− 1.06	11	82	[76]
Ultra-small SnO	0.5 M $KHCO_3$	− 0.86	20	66	[77]
SnO_2 nanosheets	0.1 M $KHCO_3$	− 1.2	16	84	[78]
Mesoporous SnO_2	0.1 M $KHCO_3$	− 1.06	16.5	82	[76]
SnO_2/hollow carbon spheres	0.1 M $KHCO_3$	− 1.2	20	62	[79]
SnO_2 nanosheets/carbon cloth	0.5 M $NaHCO_3$	− 1.0	50	87	[80]
Anodized Sn	0.1 M $KHCO_3$	− 1.0	7.2	95	[81]
AgSn/SnO_x	0.5 M $NaHCO_3$	− 0.8	16	80	[73]
Cu_2S	0.1 M $KHCO_3$	− 0.9	19	87	[82]
CuS_x	0.1 M $KHCO_3$	− 0.85	11.9	75	[83]
S-modified Cu	0.1 M $KHCO_3$	− 0.8	20	80	[84]
SnS_2/RGO	0.5 M $NaHCO_3$	− 1.4 (vs. Ag/AgCl)	13.9	84	[31]
Bi_2S_3–Bi_2O_3@rGO	0.1 M $KHCO_3$	− 0.9	3.8	90	[85]
Bi dendrite	0.5 M $KHCO_3$	− 1.14	41	38	[86]
Bi_2O_3 nanoparticles	0.5 M $NaHCO_3$	− 1.2	20	91	[87]
Bi_2O_3 nanosheets	0.1 M $KHCO_3$	− 1.056	7.8	97	[88]

selectivity and electrode activity, good production rate of $HCOO^-$ can be obtained on the SnS/pCNC electrode (Fig. 7d). The maximum production rate of $HCOO^-$ is 47.5 mg cm^{-2} h^{-1} at − 1.2 V.

According to the literature, the pathways for the CO_2RR to $HCOO^-$ on SnS_x catalysts are characterized by a reversible CO_2/CO_2^- process prior to a rate-determining chemical step, suggesting the sulfide could facilitate CO_2 reduction, probably through the stabilization of the CO_2^- intermediate [31]. It is reported that when CO_2^- intermediate binds to p-block elements, particularly S, a singly occupied p orbital can stabilize the electron localized in the $2p_z$ orbital of C associated with CO_2^- [70]. Hwang et al. [71] also showed that the enhanced catalytic behavior of Ag nanoparticle on carbon support was associated with the cysteamine anchoring agent, which developed Ag–S interaction. The Ag–S interaction induces surface localization of the unpaired electron, resulting in an enhanced stabilization of the CO_2^- intermediate. Based on the above discussion and literature including computational, electrokinetic and in situ analysis [34, 72–74], the formation of $HCOO^-$ goes through the following pathway: (1) a fast step to form CO_2^- radical anion via a one-electron transfer, which is bonded to the electrode surface through O atom, (2) a second rate-determining step to protonate CO_2^- on the carbon atom, leading to the formation of a $HCOO^·$ intermediate, and (3) a third step for a second electron transfer, resulting in the $HCOO^-$ product.

We use electrodes with an active area of 1.5 cm^2, and the CO_2 flow rate is 25 mL min^{-1}. The single-pass conversion of CO_2 can be calculated according to the following equation, single-pass conversion = production rate × active area/(flow rate/V) in which production rate is the $HCOO^-$ yielding rate (mg cm^{-2} min^{-1}); active area is the effective area of electrode (cm^2); flow rate is the rate of CO_2 gas (mL min^{-1}); and V is the volume of 1 mol of idea gas (ml mmol^{-1}). The calculated single-pass conversion of CO_2 is 2.36%. This value is relatively low with respect to our previous work where 22% of single-pass conversion was obtained [75], since the process was not optimized for this purpose in the present work. Further work will be focused on the improving of the single-pass CO_2 conversion in order to simplify the down-stream separations.

Concisely, the SnS species-decorated pCNC shows good selectivity and activity for the electrosynthesis of $HCOO^-$ from CO_2 reduction. Particularly, the small size and low percentage of Sn species permit good utilization efficiency of metal, lowering the cost of the material and allowing its production at large scales.

Conclusions

This work presents the experimental results on the development of novel and low-cost catalytic material for CO_2 electroreduction in aqueous solution. We recovered conductive CNC as microstructured carbon support via pyrolysis and then deposited nanosized SnS nanocrystals on carbon surface by employing a green and fast microwave-assisted hydrothermal process. The latter technique allows uniform decoration of the carbon surface with 17.9 wt% of SnS, as confirmed by various characterizations including morphological, structural, surficial and thermal analyses.

The electrocatalytic performance of the nanocomposite was thoroughly evaluated, showing high selectivity and activity for converting CO_2 to $HCOO^-$. The high performance and low metal loading of the catalyst allow high-efficiency utilization of metal, consequently further reducing the cost of materials. Furthermore, the fabrication methods are sustainable and scalable, evidencing the promising potential of the proposed catalyst to be implemented into industrially relevant processes for electrosynthesis of $HCOO^-$ from the CO_2RR.

Author contributions

NG contributed to conceptualization; NG and JZ provided methodology; NG, MB, NM, CFP, and JZ carried out formal analysis; JZ and NM performed investigation; CFP provided resources; MB, JZ, and NM performed data curation; NG, MB, NM, CFP, and JZ performed writing—original draft preparation; NG, MB, NM, CFP, and JZ performed writing—review and editing; NG, MB, NM, CFP, and JZ performed visualization; NG and JZ performed supervision; CFP carried out project administration. Authors have read and agreed to the published version of the manuscript.

Funding

Open access funding provided by Politecnico di Torino within the CRUI-CARE Agreement.

Data and code availability

Not Applicable.

Declarations

Conflict of interest The authors declare no conflict of interest.

Ethical approval Not Applicable.

Supplementary Information The online version contains supplementary material available at https://doi.org/10.1007/s10853-023-08925-2.

References

[1] Pirani S (2018) Burning up: a global history of fossil fuel consumption. Pluto Press, London
[2] Wang L, Chen W, Zhang D et al (2019) Chem Soc Rev 48:5310
[3] Li X, Yu J, Jaroniec M, Chen X (2019) Chem Rev 119:3962
[4] Masson-Delmotte V, Zhai P, Pirani A et al (2021) In: Contribution of working group I to the sixth assessment report of the intergovernmental panel on climate change, vol 2
[5] Keith DW, Holmes G, Angelo DS, Heidel K (2018) Joule 2:1573
[6] Wu Q, Pan M, Zhang S et al (2022) Energies 15:6666
[7] Artz J, Müller TE, Thenert K et al (2018) Chem Rev 118:434
[8] Nguyen DN (2003) SPE/EPA/DOE exploration and production environmental conferenceOnePetro
[9] Li Z, Li H, Yang S (2022) Adv Sustain Syst 6:2100380

[10] Zhu K, Li Y, Li Z, Liu Y, Wu H, Li H (2022) Chem Commun 58:12712
[11] Voormeij DA, Simandl GJ (2004) Geosci Can 31:11
[12] Alper E, Orhan OY (2017) Petroleum 3:109
[13] Rafiee A, Khalilpour KR, Milani D, Panahi M (2018) J Environ Chem Eng 6:5771
[14] Lu Q, Jiao F (2016) Nano Energy 29:439
[15] Saha P, Amanullah S, Dey A (2022) Acc Chem Res 55:134
[16] Hussain J, Jónsson H, Skúlason E (2018) ACS Catal 8:5240
[17] Jouny M, Luc W, Jiao F (2018) Ind Eng Chem Res 57:2165
[18] Aresta M, Dibenedetto A, Angelini A (2014) Chem Rev 114:1709
[19] Wu S, Yang F, Wang H, Chen R, Sun P, Chen T (2015) Chem Commun 51:10887
[20] Joó F (2008) ChemSusChem: Chem Sustain Energy Mater 1:805
[21] Enthaler S, von Langermann J, Schmidt T (2010) Energy Environ Sci 3:1207
[22] Duarah P, Haldar D, Yadav V, Purkait MK (2021) J Environ Chem Eng 9:106394
[23] Cai F, Gao D, Si R et al (2017) Electrochem Commun 76:1
[24] Zeng J, Rino T, Bejtka K et al (2020) Chemsuschem 13:4128
[25] Zeng J, Bejtka K, Di Martino G et al (2020) ChemElectroChem 7:229
[26] Zeng J, Fiorentin MR, Fontana M et al (2022) Appl Catal B 306:121089
[27] Lourenço MA, Zeng J, Jagdale P et al (2021) ACS Sustain Chem Eng 9:5445
[28] Zeng J, Jagdale P, Lourenço MAO et al (2021) Crystals 11:363
[29] Innocent B, Pasquier D, Ropital F, Hahn F, Léger J-M, Kokoh K (2010) Appl Catal B 94:219
[30] Won DH, Choi CH, Chung J, Chung MW, Kim EH, Woo SI (2015) Chemsuschem 8:3092
[31] Li F, Chen L, Xue M et al (2017) Nano Energy 31:270
[32] Chen Y, Li CW, Kanan MW (2012) J Am Chem Soc 134:19969
[33] Li Q, Rao X, Sheng J et al (2018) J CO2 Util 27:48
[34] Zhao S, Li S, Guo T et al (2019) Nano-Micro Lett 11:62. https://doi.org/10.1007/s40820-019-0293-x
[35] Zago S, Bartoli M, Muhyuddin M et al (2022) Electrochim Acta 412:140128
[36] Bartoli M, Giorcelli M, Jagdale P et al (2019) SN Appl Sci 1:1661. https://doi.org/10.1007/s42452-019-1727-2
[37] Bartoli M, Rosso C, Giorcelli M et al (2020) J Appl Polym Sci 137:48896
[38] Arrigo R, Bartoli M, Torsello D, Ghigo G, Malucelli G (2021) Mater Today Commun 28:102630. https://doi.org/10.1016/j.mtcomm.2021.102630
[39] Kim HS, Abbas MA, Kang MS, Kyung H, Bang JH, Yoo WC (2019) Electrochim Acta 304:210
[40] Habibi Y, Lucia LA, Rojas OJ (2010) Chem Rev 110:3479
[41] Vanderfleet OM, Cranston ED (2021) Nat Rev Mater 6:124
[42] Li H, Fang Z, Smith RL Jr, Yang S (2016) Prog Energy Combust Sci 55:98
[43] Huang J, Jian Y, Li H, Fang Z (2022) Catal Today 404:35
[44] Li H, Yang T, Fang Z (2018) Appl Catal B 227:79
[45] Li R, Liu F, Zhang Y, Guo M, Liu D (2020) ACS Appl Mater Interfaces 12:44578
[46] Huang Y, Deng Y, Handoko AD, Goh GK, Yeo BS (2018) Chemsuschem 11:320
[47] Giorcelli M, Bartoli M, Sanginario A et al (2021) ACS Appl Electron Mater 3:838. https://doi.org/10.1021/acsaelm.0c00971
[48] Tagliaferro A, Rovere M, Padovano E, Bartoli M, Giorcelli M (2020) Nanomaterials 10:1748
[49] Crespiera SM, Amantia D, Knipping E et al (2016) RSC Adv 6:57335
[50] Zeng J, Nair JR, Francia C, Bodoardo S, Penazzi N (2014) Solid State Ion 262:160
[51] Vankova S, Francia C, Amici J et al (2017) Chemsuschem 10:575
[52] Zeng J, Fontana M, Sacco A, Sassone D, Pirri CF (2022) Catal Today 397:463
[53] Torsello D, Ghigo G, Giorcelli M, Bartoli M, Rovere M, Tagliaferro A (2021). Carbon Trends 4:100062. https://doi.org/10.1016/j.cartre.2021.100062
[54] Greyson EC, Barton JE, Odom TW (2006) Small 2:368
[55] Nair P, Nair M, Campos J (1993) J Electrochem Soc 140:539
[56] Tuinstra F, Koenig JL (1970) J Chem Phys 53:1126. https://doi.org/10.1063/1.1674108
[57] Ferrari AC, Robertson J, Ferrari AC, Robertson J (2004) Philos Trans R Soc Lond Ser A: Math Phys Eng Sci 362:2477. https://doi.org/10.1098/rsta.2004.1452
[58] Eom Y, Son SM, Kim YE, Lee J-E, Hwang S-H, Chae HG (2019) Carbon 150:142
[59] Savi P, Cirielli D, di Summa D, Ruscica G, Sora IN (2019) In: 2019 IEEE 5th international forum on research and technology for society and industry (RTSI). IEEE
[60] Tamborrino V, Costamagna G, Bartoli M et al (2021) Fuel 296:120693
[61] Ravi S, Zhang S, Lee Y-R et al (2018) J Ind Eng Chem 67:210
[62] Sahu S, Rani Sahoo P, Patel S, Mishra B (2011) J Sulfur Chem 32:171
[63] Sacco A, Zeng J, Bejtka K, Chiodoni A (2019) J Catal 372:39
[64] Zeng J, Bejtka K, Ju W et al (2018) Appl Catal B 236:475

[65] Zhang S, Kang P, Meyer TJ (2014) J Am Chem Soc 136:1734
[66] Zhao Y, Liang J, Wang C, Ma J, Wallace GG (2018) Adv Energy Mater 8:1702524. https://doi.org/10.1002/aenm.201702524
[67] Del Castillo A, Alvarez-Guerra M, Solla-Gullón J, Sáez A, Montiel V, Irabien A (2015) Appl Energy 157:165. https://doi.org/10.1016/j.apenergy.2015.08.012
[68] Dutta A, Kuzume A, Rahaman M, Vesztergom S, Broekmann P (2015) ACS Catal 5:7498. https://doi.org/10.1021/acscatal.5b02322
[69] Kuzume A, Dutta A, Vesztergom S, Broekmann P (2018) In: Wandelt K (ed) Encyclopedia of interfacial chemistry. Elsevier, Oxford
[70] Lim H-K, Shin H, Goddard WA III, Hwang YJ, Min BK, Kim H (2014) J Am Chem Soc 136:11355. https://doi.org/10.1021/ja503782w
[71] Kim C, Jeon HS, Eom T et al (2015) J Am Chem Soc 137:13844. https://doi.org/10.1021/jacs.5b06568
[72] Yoo JS, Christensen R, Vegge T, Nørskov JK, Studt F (2016) Chemsuschem 9:358. https://doi.org/10.1002/cssc.201501197
[73] Luc W, Collins C, Wang S et al (2017) J Am Chem Soc 139:1885
[74] Genovese C, Ampelli C, Perathoner S, Centi G (2017) Green Chem 19:2406. https://doi.org/10.1039/C6GC03422E
[75] Monti NBD, Fontana M, Sacco A et al (2022). ACS Appl Energy Mater 5:14788. https://doi.org/10.1021/acsaem.2c02143
[76] Bejtka K, Zeng J, Sacco A et al (2019) ACS Appl Energy Mater 2:3081. https://doi.org/10.1021/acsaem.8b02048
[77] Gu J, Héroguel F, Luterbacher J, Hu X (2018) Angew Chem Int Ed 57:2943. https://doi.org/10.1002/anie.201713003
[78] Li X, Dou S, Wang J, Wang X (2020) Chem Asian J 15:1558. https://doi.org/10.1002/asia.202000252
[79] Wang Z, Yang C, Guan A et al (2018) J Mater Chem A 6:20121
[80] Li F, Chen L, Knowles GP, MacFarlane DR, Zhang J (2017) Angew Chem Int Ed 56:505. https://doi.org/10.1002/anie.201608279
[81] Morimoto M, Fujita N, Takatsuji Y, Haruyama T (2022) Electrocatalysis 13:72
[82] He W, Liberman I, Rozenberg I, Ifraemov R, Hod I (2020) Angew Chem 132:8339
[83] Deng Y, Huang Y, Ren D et al (2018) ACS Appl Mater Interfaces 10:28572
[84] Shinagawa T, Larrazábal GO, Martín AJ, Krumeich F, Pérez-Ramírez J (2018) ACS Catal 8:837
[85] Yang X, Deng P, Liu D et al (2020) J Mater Chem A 8:2472
[86] Koh JH, Won DH, Eom T et al (2017) ACS Catal 7:5071. https://doi.org/10.1021/acscatal.7b00707
[87] Miao C-C, Yuan G-Q (2018) ChemElectroChem 5:3741. https://doi.org/10.1002/celc.201801036
[88] Liu S, Lu XF, Xiao J, Wang X, Lou XW (2019) Angew Chem Int Ed 58:13828. https://doi.org/10.1002/anie.201907674